



OPEN

Discovery of first-in-class nanomolar inhibitors of heptosyltransferase I reveals a new aminoglycoside target and potential alternative mechanism of action

Jozafina Milicaj^{1,5}, Bakar A. Hassan^{1,5}, Joy M. Cote¹, Carlos A. Ramirez-Mondragon⁴, Nadiya Jaunbocus¹, Angelika Rafalowski¹, Kaelan R. Patel², Colleen D. Castro¹, Ramaiah Muthyala³, Yuk Y. Sham^{2,4}✉ & Erika A. Taylor¹✉

A clinically relevant inhibitor for Heptosyltransferase I (HepI) has been sought after for many years because of its critical role in the biosynthesis of lipopolysaccharides on bacterial cell surfaces. While many labs have discovered or designed novel small molecule inhibitors, these compounds lacked the bioavailability and potency necessary for therapeutic use. Extensive characterization of the HepI protein has provided valuable insight into the dynamic motions necessary for catalysis that could be targeted for inhibition. Structural inspection of Kdo₂-lipid A suggested aminoglycoside antibiotics as potential inhibitors for HepI. Multiple aminoglycosides have been experimentally validated to be first-in-class nanomolar inhibitors of HepI, with the best inhibitor demonstrating a K_i of 600 ± 90 nM. Detailed kinetic analyses were performed to determine the mechanism of inhibition while circular dichroism spectroscopy, intrinsic tryptophan fluorescence, docking, and molecular dynamics simulations were used to corroborate kinetic experimental findings. While aminoglycosides have long been described as potent antibiotics targeting bacterial ribosomes' protein synthesis leading to disruption of the stability of bacterial cell membranes, more recently researchers have shown that they only modestly impact protein production. Our research suggests an alternative and novel mechanism of action of aminoglycosides in the inhibition of HepI, which directly leads to modification of LPS production in vivo. This finding could change our understanding of how aminoglycoside antibiotics function, with interruption of LPS biosynthesis being an additional and important mechanism of aminoglycoside action. Further research to discern the microbiological impact of aminoglycosides on cells is warranted, as inhibition of the ribosome may not be the sole and primary mechanism of action. The inhibition of HepI by aminoglycosides may dramatically alter strategies to modify the structure of aminoglycosides to improve the efficacy in fighting bacterial infections.

Abbreviations

GT	Glycosyltransferase
CAZY	Carbohydrate-Active enZymes Database
HepI	Heptosyltransferase I
ADP-Hep	ADP- <i>L</i> -glycero- β - <i>D</i> -manno-heptose

¹Department of Chemistry, Wesleyan University, Middletown, CT 06459, USA. ²Department of Integrative Biology and Physiology, Medical School, University of Minnesota, Minneapolis, MN 55455, USA. ³Department of Experimental and Clinical Pharmacology, College Pharmacy, University of Minnesota, Minneapolis, MN 55455, USA. ⁴Bioinformatics and Computational Biology Program, University of Minnesota, Minneapolis, MN 55455, USA. ⁵These authors contributed equally: Jozafina Milicaj and Bakar A. Hassan. ✉email: shamx002@umn.edu; eataylor@wesleyan.edu

Kdo	3-Deoxy- <i>D</i> -manno-oct-2-ulosonic acid
ODLA	O-deacylated Kdo ₂ -Lipid A
H-Kdo ₂ -Lipid A	Heptosylated Kdo ₂ -Lipid A
FDLA	Fully-deacylated Kdo ₂ -Lipid A
ADP	Adenosine diphosphate
FDHLA	Fully-deacylated heptosylated- Kdo ₂ -Lipid A
FDLA-H	Deprotonated sugar donor nucleophile
D13 + H	Protonated aspartic acid 13
TIP3P	Transferrable intermolecular potential with 3 points
RMSD	Root mean square deviation
Rgyr	Radius of gyration
RMSF	Root mean square fluctuations
PCA	Principal component analysis
DCCM	Dynamic cross correlation matrix
Amp	Ampicillin
Tet	Tetracycline
CD	Circular dichroism
T _m	Melting temperature

The ever-growing number of infections and deaths due to antibiotic resistant bacteria is a global health issue necessitating development of novel therapeutics to treat these new multi-drug resistant species. Gram-negative bacteria are more likely to develop resistance than Gram-positive bacteria¹, in part due to their complex membrane morphology and the extracellular polymeric substances (EPS) which decrease the permeability of xenobiotics and improve surface adhesion². EPS provide structural integrity to the intracellular matrix of a bacterial biofilm, which further enhances their resistance to hydrophobic antibiotics^{3,4}. Lipopolysaccharide (LPS) is a major component of Gram-negative EPS making up approximately 30% of the outer membrane while facilitating multiple purposes including enabling cellular motility, adhesion, and nutrient retrieval^{5,6}. Cellular exposure to an extracellular threat such as an antibiotic or antigen, can trigger modification of LPS to further fortify the outer membrane leaflet, a common resistance mechanism known to reduce membrane permeability^{4,7,8}.

Previous studies have shown that when the LPS pathway genes are knocked out, it causes increased susceptibility to antibiotics, reduced cellular motility, reduced cellular adhesion, and in some cases was fatal to the cell⁹. This information taken with the knowledge that the inner oligosaccharide core biosynthesis of LPS is conserved among all Gram-negative bacteria, reveals a potential target that can be exploited for therapeutic design¹⁰. The first step in the LPS core biosynthetic pathway is catalyzed by Heptosyltransferase I (HepI), also known as WaaC (or RfaC), which is responsible for the transfer of a heptose moiety onto the first Kdo of Kdo₂-Lipid A (Kdo: 3-deoxy-*D*-manno-oct-2-ulosonic acid)¹¹ (Fig. 1A). HepI is a GT-B glycosyltransferase enzyme with two Rossmann-like domains (connected by a linker region); each domain binds one of the two enzymatic substrates (the N-terminal domain binds the nucleophilic Kdo₂-Lipid A, while the C-terminal domain binds the electrophilic sugar donor ADP-*L*-glycero- β -*D*-manno-heptose, or ADPH) (Fig. 1B).

Previous attempts at inhibiting HepI have yielded micromolar inhibitors, similar to the K_M values of substrate, which aren't sufficiently potent for further development and optimization^{7,12}. Grizot et al. demonstrated a fluorine substituted ADPH analog that performed well as a competitive inhibitor of the sugar donor binding site with a mid-micromolar affinity; this compound was later used in a liganded crystal structure of the protein (PDB: 2H1H)¹¹. Moreau et al. in 2008 ran the first virtual high-throughput screening with 5 million molecules to generate a small library of compounds, which were further evaluated experimentally to determine micromolar affinity for the best ligands⁷. Tikad and coworkers in 2016 took a novel approach by generating a series of sugar substituted Kdo glyco-clusters and managed to achieve low micromolar inhibition with HepI; however, there seemed to be a weak bioavailability of these compounds due to their large size which violated Lipinski's rules¹³. The authors also observed aggregation of HepI with their tightest binding inhibitor in vitro making the overall success of their experimental findings unclear. In 2018, Nkosana et al. synthesized monosaccharide lipid A analogs to probe the sugar acceptor binding site yielding high micromolar inhibitors of HepI. While these inhibitors had poor potency, they were the first to demonstrate that HepI could be inhibited by compounds with non-competitive inhibition mechanisms¹⁴.

The inability to potently inhibit HepI in these endeavors suggests that alternative strategies, including seeking non- and un-competitive inhibitors that impact the protein conformational changes may be necessary to effectively inhibit it. HepI, like other GT-B enzymes of its family, has been predicted to undergo an open-to-closed transition about a hinge region, with various studies from our lab (both experimental and computational) showing that the interconversion is driven by ligand binding. For example, studies by Czyzyk et al. which included kinetic viscosity studies, as well as fluorescence stop-flow pre-steady state kinetics, showed that enzyme dynamics are partially rate limiting and play an integral role in HepI substrate binding and catalysis¹⁵. These dynamical motions were further examined through use of HepI mutant enzymes by Cote et al. to examine residues that trigger conformational changes through a series of kinetic, circular dichroism spectroscopy and intrinsic tryptophan fluorescence studies. These experiments revealed amino acids responsible for ligand binding interactions necessary for initiating the open-to-closed transition^{16,17}. Collectively, the data described above exposed essential information about the conformational transitions of HepI that occur in the presence of an analog of its native substrate, O-deacylated Kdo₂-Lipid A (ODLA). Computational studies of HepI, in the presence and absence of its native substrates, helped to reveal an overall structural model for the conformational changes occurring during catalysis which can provide powerful insights for the design of HepI inhibitors^{18,19}.

Inhibitor	Mutation	k_{cat} (s^{-1}) No inhibitor	K_M (μM) No inhibitor	k_{cat} (s^{-1})	K_i (μM)	Type of inhibition with ODLA
Amikacin	WT	0.36 ± 0.02	2.9 ± 0.6	0.138 ± 0.001	4.258 ± 0.631	N/A
Neomycin				0.156 ± 0.007	1.643 ± 0.284	Competitive
Kanamycin B				0.149 ± 0.007	0.99 ± 0.119	Competitive
Tobramycin				0.15 ± 0.005	1.125 ± 0.212	Mixed competitive
Streptomycin				0.162 ± 0.008	0.595 ± 0.09	Non-competitive
Tobramycin	R60A	0.198 ± 0.009	6 ± 1	0.111 ± 0.013	3.4 ± 0.631	N/A
Tobramycin	R120A	0.32 ± 0.03	15 ± 3	0.829 ± 0.044	0.422 ± 0.186	N/A
Streptomycin	R60A	0.198 ± 0.009	6 ± 1	0.149 ± 0.013	6.254 ± 5.427	N/A
Streptomycin	R61A	0.36 ± 0.01	2.5 ± 0.4	0.142 ± 0.031	7.89 ± 3.592	N/A
Streptomycin	R63A	0.41 ± 0.03	10 ± 2	0.198 ± 0.024	6.663 ± 0.699	N/A
Streptomycin	K64A	0.33 ± 0.02	8 ± 2	0.117 ± 0.009	5.756 ± 0.485	N/A

Table 1. Kinetic parameters of HepI in the presence/absence of aminoglycoside inhibitors and mutants of binding residues.

Structural similarity inspection, combined with experimental validation, enabled the discovery of five commercially available aminoglycosides that inhibit HepI with low micromolar to high nanomolar affinity (Fig. 2, Table 1). The prior consensus in the literature stated that aminoglycosides act through the disruption of protein synthesis, thereby preventing the translation of membrane proteins and leading to changes in the cell surface morphology and damage to the cytoplasmic membrane^{20–24}. Recently, researchers have demonstrated, using single-molecule spectroscopic methods, that aminoglycosides only slow protein synthesis and don't inhibit it fully, therefore suggesting that the bactericidal activity of aminoglycosides is not related to ribosomal inhibition²⁵. Herein, we propose an alternative mechanism of action of aminoglycosides through the potent inhibition of HepI and disruption of lipopolysaccharide biosynthesis. This novel mechanism of action has been demonstrated through detailed kinetic analyses of enzyme inhibition, circular dichroism spectroscopy, intrinsic tryptophan fluorescence, molecular dynamic simulations and in vivo analysis of LPS biosynthesis and cell growth. These aminoglycosides resemble the tetrasaccharide core of Kdo₂-Lipid A, and based upon kinetic and computational methods we reveal that some bind competitively in the N-terminal domain, while others bind noncompetitively in a previously identified binding pocket located near the HepI hinge region¹⁹. We illustrate that multiple ligand binding modes prove effective in disruption catalysis of this highly dynamic GT-B protein.

Results

Kinetic analysis of putative inhibitors. Inhibition constant (K_i) values were determined for each aminoglycoside by varying inhibitor concentration at constant substrate concentration for all five putative inhibitors (Fig. 3). All compounds inhibited HepI to varying degrees as shown in Table 1, exhibiting low micromolar to high nanomolar affinity which is noteworthy for a series of first-generation inhibitors. Amikacin was the most ineffective inhibitor, with a K_i of $4.3 \mu M$ while neomycin and tobramycin exhibited slightly better K_i values of 1.6 and $1.1 \mu M$, respectively. The best two inhibitors were kanamycin and streptomycin both of which displayed high nanomolar inhibition constants at 990 nM and 595 nM, respectively. Tobramycin and streptomycin were two potent inhibitors with different structural scaffolds, tobramycin having a trisaccharide structure made up of exclusively 6-membered rings, while streptomycin is a trisaccharide with a ribose ring among the 6-membered rings (Fig. 2).

Further inhibition experiments were performed with the four best inhibitors, two of each structural category: neomycin, tobramycin, kanamycin, and streptomycin. These were performed at multiple substrate concentrations with varying inhibitor concentrations to determine the type of inhibition using Lineweaver–Burk, Dixon and Cornish-Bowden analyses (Fig. 3A–F). By Lineweaver–Burk analysis tobramycin appears to be competitive with ODLA; however, upon careful inspection of the data, the curves do not intersect exactly at the y-axis which led to the need for additional analysis methods (Fig. 3D). Reanalysis of the data with the Dixon equation yielded a plot that was again ambiguous, where competitive and non-competitive mechanisms couldn't be distinguished because the lines intersect very close to the x-axis (Fig. 3E). The Cornish-Bowden method provided the necessary clarification of the inhibition type by yielding a plot that was characteristically mixed-competitive; if the inhibitor had been purely competitive in nature, the curves would have remained parallel with the Cornish-Bowden analysis (Fig. 3F). Using the mixed-model of inhibition to parse out the types of inhibition that contribute to the mixed profile of tobramycin with ODLA, we calculated an α value greater than one which suggests a competitive/non-competitive combination. Both kanamycin and neomycin also demonstrate competitive inhibition against ODLA using the same three analysis methods (Supplemental Fig. 4).

Tobramycin displays uncompetitive inhibition against ADPH, corroborated by all three analysis methods (Supplemental Fig. 2D–F). This is unsurprising because ODLA and ADPH have two distinct binding sites and tobramycin is unlikely to compete with both simultaneously due to its size. Thus, it is possible that tobramycin may bind to a region of the protein that is only accessible upon structural rearrangements after ADPH binding. The competition of tobramycin with ODLA was further investigated by examining changes in K_i values of tobramycin using mutant HepI constructs previously identified to alter the binding of ODLA¹⁷ (Supplemental

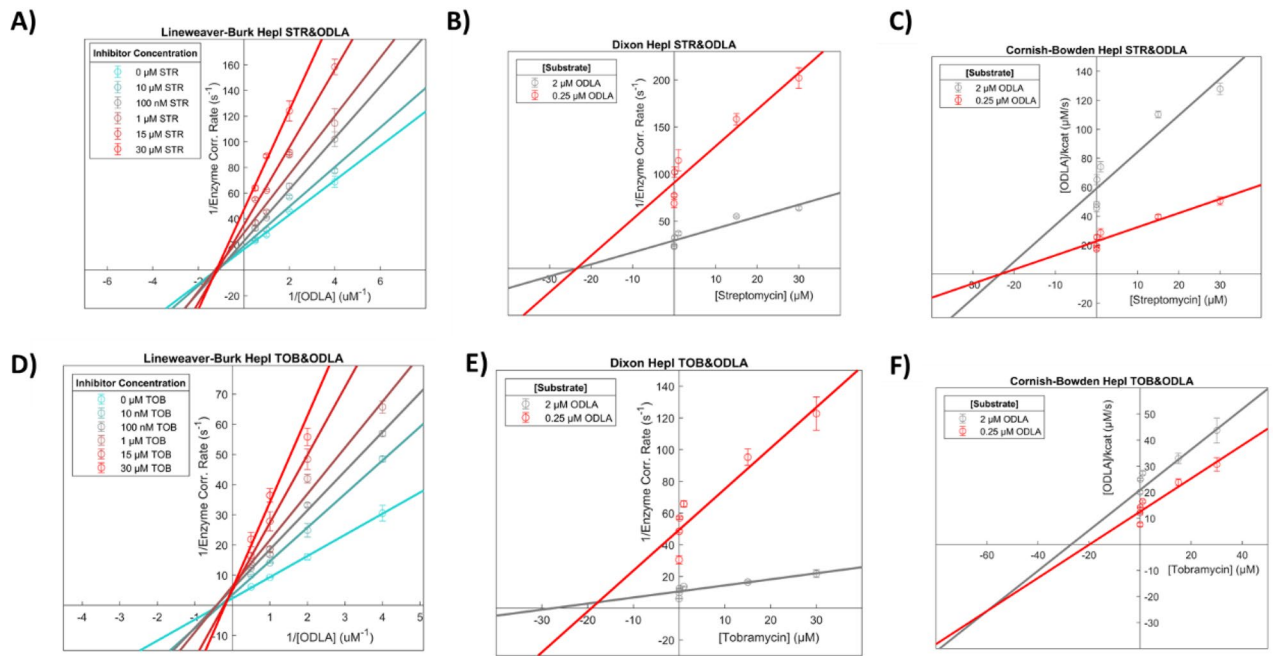


Figure 3. Kinetic analysis plots of (A–C) Streptomycin and (D–F) Tobramycin in the presence of ODLA.

Fig. 5E–F, Table 1). Specifically, mutation of the positively charged residues Arginine 60 and 120 to Alanine resulted in alterations of tobramycin inhibition of HepI (Table 1). The HepI R60A mutant exhibited a K_i approximately tenfold weaker relative to the WT, while the R120A demonstrated a K_i ~ twofold tighter than the WT.

Streptomycin exhibited non-competitive inhibition against both ODLA and ADPH, which was unambiguously evident with all three analysis methods (Fig. 3A–C, Supplemental Fig. 3D–F). Streptomycin binding to the enzyme was also investigated by way of K_i analysis using mutant forms of HepI including: R60A, R61A, R63A, and K64A (Table 1, Supplemental Fig. 5A–D). Varying concentrations of Streptomycin with all four mutant forms increased the K_i values an order of magnitude suggesting that these residues were not just proximal to the Streptomycin binding site but are also mediating the binding of the compound.

Circular dichroism thermal analysis. Since kinetic analyses indicate that tobramycin is partially competitive with ODLA for binding, circular dichroism studies were performed to assess if tobramycin disrupts the previously observed ODLA-induced thermal stabilization of HepI¹⁷. Previous studies of HepI WT revealed that the apo protein melts at around 37 °C and unfolds ~ 80% from the fully folded, whereas in the presence of ODLA, HepI shows an increase in thermal stability and melts above 95 °C (Fig. 4, Supplemental Fig. 6A–B). The addition of ADPH to WT HepI does not induce any changes in the melting temperature but does destabilize the protein to allow it to unfold fully (~ 100%). Unsurprisingly, HepI in the presence of the heptosylated ODLA (ODHLA) product behaves like HepI and ODLA with no observable melting event below 95 °C and HepI with ADP melts similarly to HepI with ADPH (Supplemental Fig. 8).

The HepI•tobramycin complex has a T_m of ~ 37 °C with a 20% increase in unfolding as compared to apo (Fig. 3, Supplemental Fig. 7D), suggesting an induced destabilization of the enzyme. The addition of tobramycin to the HepI•ODLA complex disrupts the ODLA-induced thermal stabilization resulting in a protein complex that melts at around ~ 58 °C and unfolds to about 70% (Fig. 4, Supplemental Figs. 6C, 7, 8). HepI with ADPH and tobramycin showed no changes from HepI with ADPH alone. These findings are corroborated by the kinetic analysis of tobramycin being a mixed-competitive inhibitor against ODLA. A CD melt analysis of the HepI•tobramycin complex with each of the products behaves like their substrate counterparts.

HepI with streptomycin melts at 37 °C with a ~ 20% increase in unfolded protein in comparison to apo and no discernable difference in secondary structure (Supplemental Fig. 6C, Supplemental Fig. 7A). Streptomycin in the presence of either substrate or product appears no different from substrate or product alone (Supplemental Fig. 7C–D, Supplemental Fig. 8B). This aligns well with the kinetics data that suggests that streptomycin is non-competitive with both substrates. The inhibitor is free to bind to any form of HepI (E, E•S, E•S₂, E•P₂, E•P) and interrupt chemistry.

Intrinsic tryptophan fluorescence. Characteristic behavior of HepI in fluorescence studies have shown that formation of the HepI•ODLA complex results in a 6 nm blue shift in the HepI Tryptophan (Trp) emission spectra (Fig. 5A). This method was a good reporter of global protein rearrangements that caused Trps to become less solvent exposed due to ODLA binding. If tobramycin disrupted the thermal stability of HepI with ODLA it was then hypothesized that it would truncate the blue shift however, it did not (Fig. 5B, Supplemental Fig. 10B). HepI with tobramycin did not alter the λ_{max} and when adding tobramycin to the HepI•ODLA com-

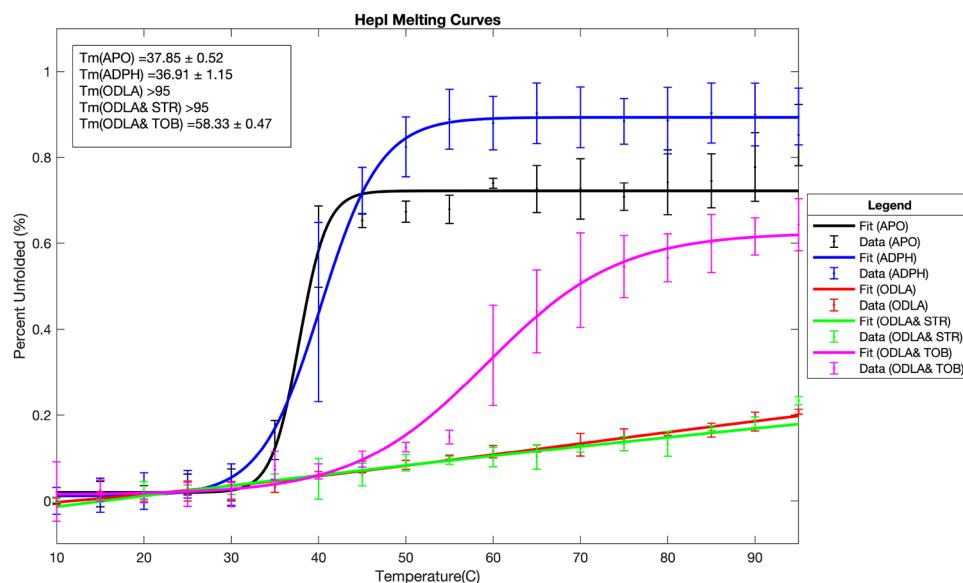


Figure 4. HepI melt curves in the presence of substrates and aminoglycoside inhibitors.

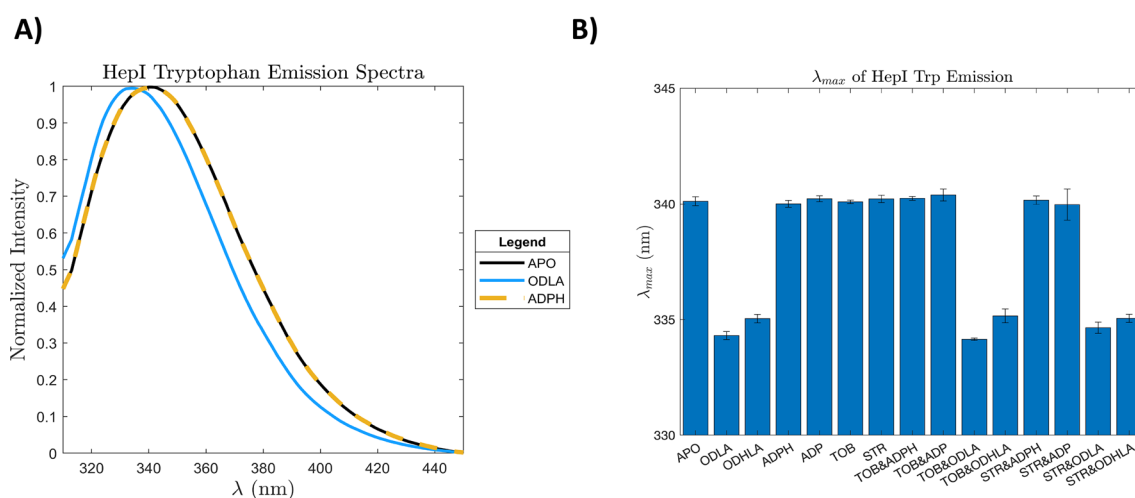


Figure 5. HepI tryptophan fluorescence emission (A) spectra and (B) λ_{max} in the presence/absence of substrates, products and inhibitors.

plex, a 6 nm blue shift was still observed. Furthermore, the same phenomenon was observed with streptomycin where the substrate induced blueshift was unperturbed. HepI•tobramycin and HepI•streptomycin complexes had no changes to the emission spectra with respect to HepI apo (Fig. 5, Supplemental Fig. 10).

Inhibitor docking and protein-inhibitor interactions dynamics. To gain a better understanding of the possible interactions between HepI and these aminoglycoside inhibitors, we turned to docking and molecular dynamics simulations guided by our experimental evidence. While experiments were performed with ODLA, a fully deacylated analog of Kdo₂-Lipid A (FDLA) was used for all computational studies (Fig. 1A). Docking experiments showed binding poses of tobramycin to the HepI•ADPH•FDLA and HepI•ADPH complex which revealed a pocket that is between the FDLA and the heptose portion of the ADPH (Fig. 6C). Furthermore, streptomycin docked to a pocket that is below the adenine ring of ADPH in the HepI•ADPH•FDLA complex (Fig. 6B). Binding free energies for tobramycin and streptomycin are outlined in Supplemental Table 3.

Simulations of HepI, HepI•ADPH•FDLA, HepI•ADP•FDHLA, HepI•ADPH•FDLA•Tobramycin, HepI•ADPH•Tobramycin, HepI•ADPH•FDLA•Streptomycin, HepI•ADP•FDHLA•Tobramycin, HepI•ADP•FDHLA•Streptomycin were performed for 100 ns, each (Supplemental Table 1). Stability of each system was determined by the average backbone root mean square deviation (RMSD) and the C-alpha radius of gyration (CaR_{gyr}). The average RMSD of all the systems coalesce to a value under 2 Å (Supplemental Figs. 11A–14A, Supplemental Table 2). As demonstrated in Supplemental Table 2, the average RMSD for HepI substrate

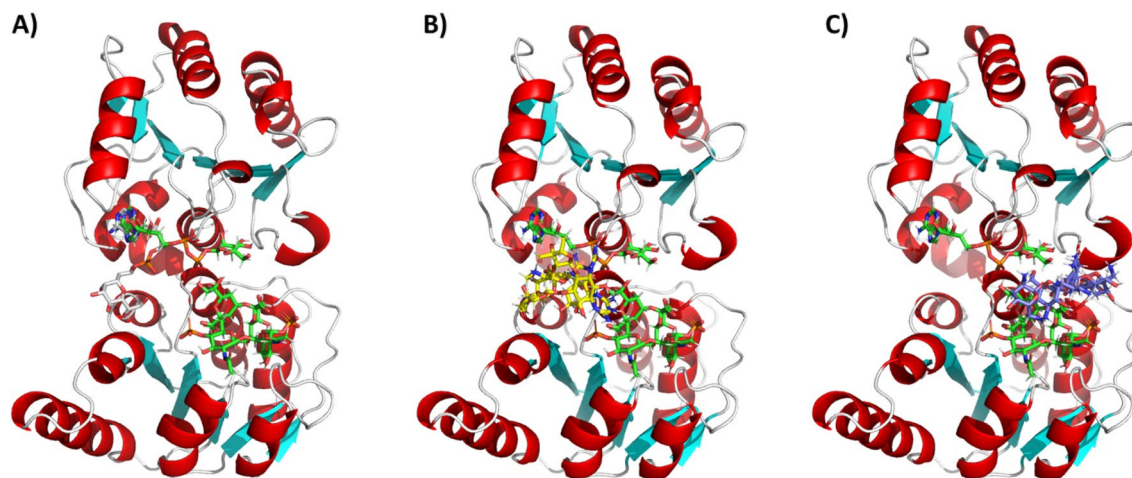


Figure 6. (A) Model of HepI•ADPH•FDLA complex with the native substrates (green) and the original pseudo phosphonate derivative (white) and (B) the top two binding poses for Streptomycin (yellow) and (C) Tobramycin (blue).

ternary complex, in the presence of tobramycin, or streptomycin are $1.84 \pm 0.23 \text{ \AA}$, $1.88 \pm 0.30 \text{ \AA}$, $1.84 \pm 0.25 \text{ \AA}$, respectively. Meanwhile, the average RMSD for HepI product complex, in the presence of tobramycin and streptomycin are $1.62 \pm 0.26 \text{ \AA}$, $1.59 \pm 0.33 \text{ \AA}$, and $1.62 \pm 0.26 \text{ \AA}$, respectively. The R_{gyr} for the HepI ternary complex, in the presence of tobramycin and streptomycin are $21.13 \pm 0.16 \text{ \AA}$, $21.23 \pm 0.12 \text{ \AA}$, and $21.28 \pm 0.16 \text{ \AA}$, respectively. In the HepI product ternary complex and in the presence of tobramycin and streptomycin, the average R_{gyr} is $21.09 \pm 0.16 \text{ \AA}$, $21.32 \pm 0.90 \text{ \AA}$, and $21.16 \pm 0.14 \text{ \AA}$, respectively.

Neither metrics display large structural deviation over time, indicative of a tightly bound stabilized closed complex. Most residues in the protein display very little fluctuations and only a handful of residues exhibit fluctuations greater than 1.5 \AA as determined by the C-alpha root mean square fluctuation ($C_{\alpha}\text{RMSF}$) (Supplemental Table 2, Supplemental Fig. 11A/B-14A/B), as is consistent with prior studies of the HepI apo and substrate complexes¹⁹. The HepI•ADPH•FDLA complex has residues with greater than 1.5 \AA fluctuations in the N_3 loop (63–69), C_1 loop (207,209), and $C_{\alpha 6}$ (300,301,317–324). Similarly, the HepI•ADPH•FDLA•tobramycin displays nearly identical regions of greater than 1.5 \AA fluctuations including residues in $N_{\alpha 3}$ (63–69,71), C_1 loop (187), $C_{\alpha 1}$ (207,209), $C_{\alpha 2}$ (231), C_5 loop (280), $C_{\alpha 5}$ (284–286), and $C_{\alpha 6}$ (300,301,317–324). Finally, the HepI•ADPH•FDLA•streptomycin complex, residues with greater than 1.5 \AA fluctuations include $N_{\alpha 3}$ (62–69,72), N_6 loop (135–136), $C_{\alpha 1}$ (207), C_5 loop (280), $C_{\alpha 5}$ (285–288), and $C_{\alpha 6}$ (300,317–324). However, in the presence of the products, dynamic residues include $N_{\alpha 3}$ (60–61,63–73,84), N_6 loop (137), $C_{5/6}$ loop (289), and $C_{\alpha 6}$ (317–320). Furthermore, tobramycin in the presence of products, HepI•ADP•FDHLA•tobramycin, has nearly identical dynamic residues which include $N_{\alpha 3}$ (61–77,84), $N_{\alpha 6}$ (136–137,156–158), $C_{\alpha 5}$ (286), $C_{5/6}$ loop (291–292), and $C_{\alpha 6}$ (318–320). On the other hand, streptomycin in the presence of the products, HepI•ADP•FDHLA•streptomycin, has fewer dynamic residues that include $N_{\alpha 3}$ (63–73) and $C_{\alpha 6}$ (318–320). The RMSF is useful for highlighting residues with large fluctuations but can be difficult for discerning small differences in fluctuations however, taking the difference of RMSFs provides relative fluctuations that may have otherwise gone unnoticed. The ΔRMSF for the HepI ternary complex in the presence of tobramycin or streptomycin relative to the HepI ternary complex in the absence of inhibitors displays changes in $N_{\alpha 4}$, $N_{\alpha 6}$, and $C_{\alpha 5}$ (Supplemental Fig. 11C–14C, Supplemental Table 2).

As stated previously, streptomycin occupies a pocket below the adenine ring of the ADPH and adjacent to the FDLA (Fig. 6B), somewhat near the linker that connects the N- and C-terminal Rossmann-like domains. Streptomycin maintains a relatively stable position throughout the 100 ns trajectory. A ligand interaction diagram for the last frame of a representative simulation reveals only one potential hydrogen bonding partner, S10 (Fig. 7A). Upon further analysis, residues with an average minimum distance of less than 3.5 \AA to streptomycin include ones in $N_{\alpha 1}$ (9–11), N_2 loop (38,40,41), $N_{\alpha 3}$ (60,63,64), $C_{\alpha 1}$ (188–190), and $C_{\alpha 2}$ (218–219,221–222) (Fig. 7C). The average minimum distance of streptomycin to ADPH or FDLA is less than 2 \AA . The streptomycin C1'–6' carbons are closest to the second KDO sugar on the C4 phosphate side. In contrast, tobramycin binds to a pocket sandwiched between the heptose moiety of ADPH and the FDLA (Fig. 6C). A ligand interaction diagram for tobramycin reveals an electrostatic attraction between a charged primary amine on tobramycin and the putative catalytic residue D13 (Fig. 7B). Residues that have an average minimum distance of less than 3.5 \AA to tobramycin include $N_{\alpha 1}$ (13), $N_{\alpha 5}$ (120), $N_{\alpha 6}$ (136–137,140,143), $C_{\alpha 1}$ (188–189,191–192), and $C_{\alpha 5}$ (281–283,286–287) (Fig. 7D). In this case, tobramycin is stacked directly above FDLA and has average minimum distance less than 2 \AA , whereas the ADPH is greater than 2 \AA (Fig. 7D). Tobramycin C1'–6" sugar stacks on top of the terminal KDO sugar, whereas the C1-6 and C1'-6' sugar/pseudosugar stack with the heptose portion of ADPH.

Comparing the average pairwise distance between atoms of the substrates and inhibitors reveals electrostatic interactions between the phosphates of the substrates and the amines of the inhibitors. The average distance between the charged secondary amine on the C2" carbon of streptomycin and the alpha phosphate oxygens of ADPH is $3.7 \pm 1.0 \text{ \AA}$ (Supplemental Fig. 15A,C). The primary amine of the streptomycin guanidinium group on the C8' carbon is $7.6 \pm 0.9 \text{ \AA}$ from the beta phosphate oxygens of ADPH. Relative to C4 GlcNAc phosphate

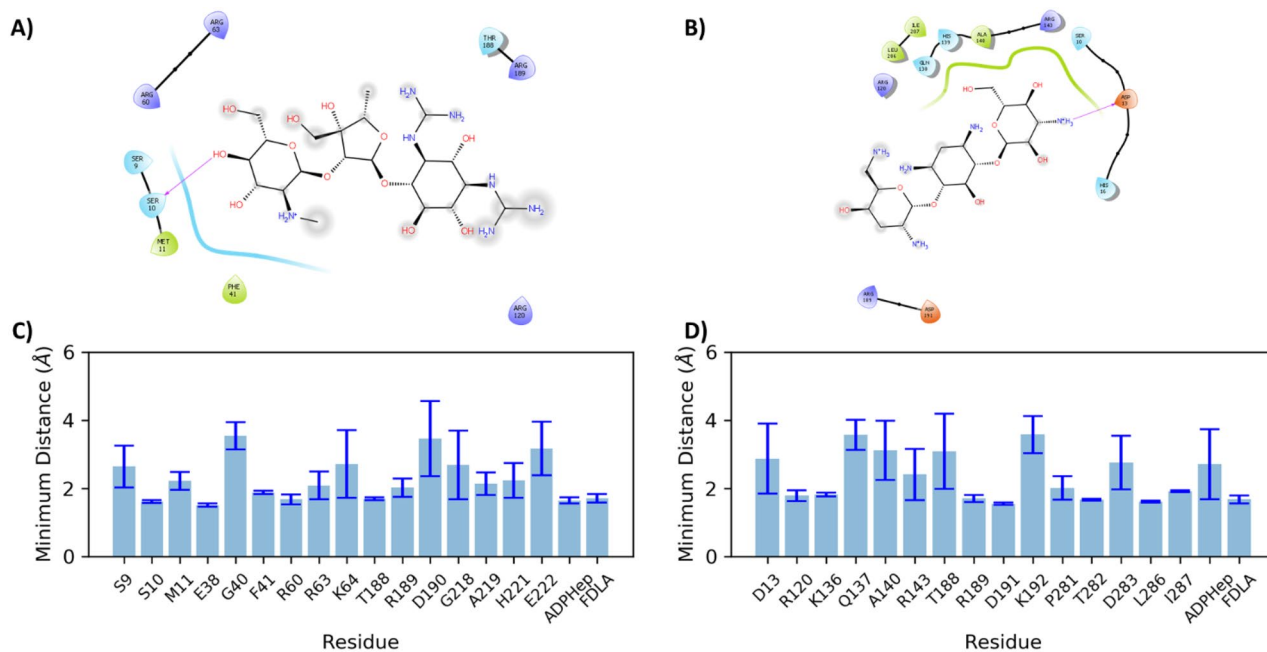


Figure 7. (A) Streptomycin Ligand Interaction Diagram (B) Tobramycin Ligand Interaction Diagram (C) Residues with minimum distance < 3.5 Å from Streptomycin and (D) Residues with minimum distance < 3.5 Å from Tobramycin.

oxygen of the FDLA, the streptomycin primary and secondary amines on the C7' carbon are 6.8 ± 1.1 Å and 6.8 ± 1.5 Å, respectively. The tobramycin charged primary amine on the C6'' carbon is 4.5 ± 0.9 Å from the C1 GlcNAc phosphate oxygens of FDLA. In the binary complex, the tobramycin primary amine is 3.3 ± 0.3 Å from the beta phosphate oxygens of ADPH.

In vivo assessment of LPS modification. To examine differences in bacterial growth rates as a result of aminoglycoside treatment, a growth challenge assay was established in a 96-well plate format using varying concentrations of inhibitor with a HepI containing *E. coli* K12 bacterial strain. As shown in Supplemental Fig. 19, increasing concentrations of tobramycin or streptomycin challenges the growth of *E. coli* K12 over an 18-h period. Growth rates decrease significantly and plateau at a maximum level of growth as shown in Fig. 9. As validated through previous works as well²⁵, the challenge presented by the introduction of aminoglycosides to *E. coli* is bactericidal and not bacteriostatic therefore growth effects are non-recoverable.

The samples grown in these challenge assays were simultaneously examined for alteration of LPS biosynthesis through gel electrophoresis studies of extracted lipids. Total bacterial cell surface lipids were extracted from 4×10^8 cells per sample (as determined by OD₆₀₀) so as to ensure that the any observable changes in lipid abundance were due to changes in extracellular polysaccharide biosynthesis and not due to changes from cell growth differences. In the presence of Tobramycin, LPS production was observed to decrease proportionally to aminoglycoside concentrations over the range of 5–7 ng/ml, with no LPS detectible at concentrations of 7.5 ng/ml or higher (Supplemental Fig. 20A). In the presence of Streptomycin, LPS production is relatively constant at low concentrations and then it decreases dramatically between 25 – 27.5 ng/ml concentrations (Supplemental Fig. 20B). IC₅₀ values were calculated using these silver-stained gels and are 6.4 ± 0.1 ng/mL for tobramycin and 26.2 ± 1.0 ng/mL for streptomycin (Fig. 9). These values are consistent with the K_i values determined above and the relative effect on growth rate for each of these inhibitors with *E. coli* K12.

Discussion

The pursuit of a potent, competitive inhibitor for HepI has been driven by the need to impede in vivo LPS biosynthesis for antimicrobial therapeutic design. Additionally, since Kdo₂-Lipid A induces a global conformational change in HepI, inhibiting HepI with a compound that binds competitively to the Kdo₂-Lipid A site could also lead to catalytically unproductive conformational changes in the enzyme, thereby reducing catalysis and subsequently the LPS coverage on the bacterial surface. The structural resemblance of the tetrasaccharide core of Kdo₂-Lipid A to a collection of aminoglycosides has led to the discovery of potent inhibitors for HepI.

The preliminary evaluation of the aminoglycoside library revealed two first-in-class, nanomolar inhibitors of HepI, streptomycin and kanamycin b. Kinetic and biophysical characterization of these inhibitors has revealed their mechanisms of action and binding sites. These inhibitors were grouped for evaluation based on their structural similarities to one another. Streptomycin and neomycin both have ribose rings mediating glycosidic bonds to 6-membered rings. Kanamycin b and tobramycin are both trisaccharides composed entirely of 6 membered rings. Kinetic analysis of inhibition with tobramycin revealed a mixed-competitive behavior against ODLA and uncompetitive inhibition against ADPH, corroborated by all three kinetic analysis methods, described above.

Kanamycin b showed competitive inhibition with ODLA; as a structural analog of tobramycin, kanamycin b that only differs by one hydroxyl group, we hypothesized that kanamycin's inhibitory character would resemble that of tobramycin with ADPH. In tobramycin, the proton at this position is within 2.5 Å of backbone and sidechain residues in C1, C5 and C6. This includes residues R189, which we have observed to coordinate to the phosphate of FDLA. If the hydroxyl in kanamycin is forming a hydrogen bond with R189 and disrupting this coordination with FDLA, this could provide a mechanism for the increased competitive nature of kanamycin relative to tobramycin.

Streptomycin was determined to act by a non-competitive mechanism with both native substrates, as described above. We hypothesized that the ribose ring would create a structural similarity between neomycin and streptomycin since both were nanomolar affinity inhibitors. Interestingly, neomycin exhibited a purely nanomolar competitive mechanism for inhibiting ODLA binding to HepI, as corroborated by our kinetic analyses. Neomycin being a tetrasaccharide may adopt a binding configuration that resembles the sugar acceptor substrate (Kdo₂-Lipid A) more effectively than tobramycin and kanamycin b, which are both trisaccharides. These data suggest that a tetrasaccharide structural scaffold is more important than sugar species in inhibition competitively with ODLA (Fig. 2, Table 1). When neomycin is superimposed on the structure of FDLA, the hexoses/pseudohexoses of neomycin superficially mimic a similar configuration of the two Glucosamines and terminal KDO of FDLA (Supplemental Fig. 17).

Docking and simulations of HepI as a substrate or product ternary complex in the presence of tobramycin or streptomycin demonstrated interesting variations in binding pockets and their effects on the conformational change required prior to catalysis which allowed the generation of models for the inhibition by these two classes of inhibitors. Streptomycin occupies a binding site that is near the hinge region between the two Rossmann-like domains (Fig. 6B). This site was previously identified as the binding site of the heptose moiety of a phosphonate derivative of ADPH in a previously solved HepI pseudo-ternary substrate complex (Fig. 6A)²⁶. Additionally, in our previous simulations of HepI with ADPH (data not shown), we observed the heptose moiety flip into this pocket over the course of a 50 ns simulation. This pocket seems to accommodate sugar binding and is therefore plausible non-competitive, allosteric inhibition pocket.

Previous studies revealed that the HepI N₃ loop, adjacent to this pocket, is highly dynamic and contains multiple residues that are involved in binding of FDLA through electrostatic interactions with redundant positively charged residues. The presence of either inhibitor does not perturb the observed molecular dynamics of this region. Streptomycin instead interacts with the phosphates on the ADP-facing side of the FDLA, but rather than outcompete the positively charged arginine/lysines, the multivalent negative charges of the phosphate can accommodate interacting with the enzyme, while also interacting with streptomycin. Furthermore, this distance between the phosphate of FDLA and the positively charged amines on streptomycin are so far apart that streptomycin will have a weak influence on the FDLA from that phosphate at best (Supplemental Fig. 15A,C). The guanidinium group on streptomycin interacts with the alpha phosphates of ADPH to further provide another anchor in that site, but streptomycin is within hydrogen bonding distance to several negatively charged residues (E38, D190, E222) that replace this interaction (Fig. 7C). Therefore, streptomycin could bind to the enzyme in the absence of these two ligands by utilizing these other negatively charged residues while staying far away enough from the crucial FDLA binding residues to constitute its place as a noncompetitive inhibitor for both substrates.

Alternatively, tobramycin binds to a cleft between the heptose and the FDLA (Fig. 6C). Experimental evidence suggests tobramycin acts as mixed (competitive/noncompetitive) inhibitor with FDLA, and an uncompetitive inhibitor of ADPH. This binding site model provides a convenient location for tobramycin to interact with ADPH in an un-competitive manner while simultaneously positioning it to replace FDLA in its absence in a competitive fashion. Additionally, binding in this pocket would allow tobramycin to act as a dynamics disruptor of the open-to-closed conformational transition which would be non-competitive with ODLA or FDLA binding. Tobramycin has a positively charged amine near the FDLA phosphate with two other positively charged residues that are within 3.5 Å (Arg120, Lys136) (Fig. 7D, Supplemental Fig. 15B,C). This will lead to an unfavorable electrostatic repulsion between these positively charged residues and tobramycin. Alanine mutation of Arg120 leads to the lowering of the inhibition constant of tobramycin, which supports this hypothesis (Table 1). Alanine mutation of K136 may be able to achieve this affect without perturbing the binding of FDLA. Alternatively, the reduction in charge of tobramycin through derivatization may lead to tighter binding inhibitor with similar properties.

In our previous molecular dynamics simulations, we observed a conformational rearrangement of HepI in the presence of its products on the nanosecond timescale reminiscent of that which is expected from a GT-B prior to catalysis. Since this rearrangement occurs prior to catalysis, we used this as a proxy to computationally explore whether these inhibitors affect the ability of the enzyme to undergo the open-to-closed transition. Specifically, we calculated the distribution of the center of mass for the enzyme in the presence of each inhibitor and compared to the uninhibited enzyme¹⁹. Based on the computationally determined center of mass distributions, streptomycin has no effect on this rearrangement, whereas tobramycin hinders the closure that can be observed over these short time periods (Fig. 8).

The biophysical characterization of HepI inhibition corroborates mechanistic behavior revealed in these molecular dynamics simulations. Previous studies that investigated the residues in HepI integral to the binding of ODLA showed a series of positively charged residues found on loops flanking either side of the ODLA binding site creating vital electrostatic interactions to the substrate. These loops rearrange to accommodate the substrate by becoming more alpha helical. Proximal to these positively charged residues are W62 & 116, previously shown to make the largest contribution to the blue shift seen with ODLA binding. Uninhibited HepI exhibits a 6 nm blue shift of the tryptophan λ_{max} upon binding of ODLA, which can serve as an indirect reporter for binding and protein rearrangement caused by ODLA (Fig. 5A)¹⁷. This spectral shift is attributed in part to changes in the hydrophobicity of the residues Trp62 and Trp116, which are on loops involved in the binding of ODLA. Neither of these inhibitors affect the steady-state tryptophan fluorescence blue shift, which is consistent with

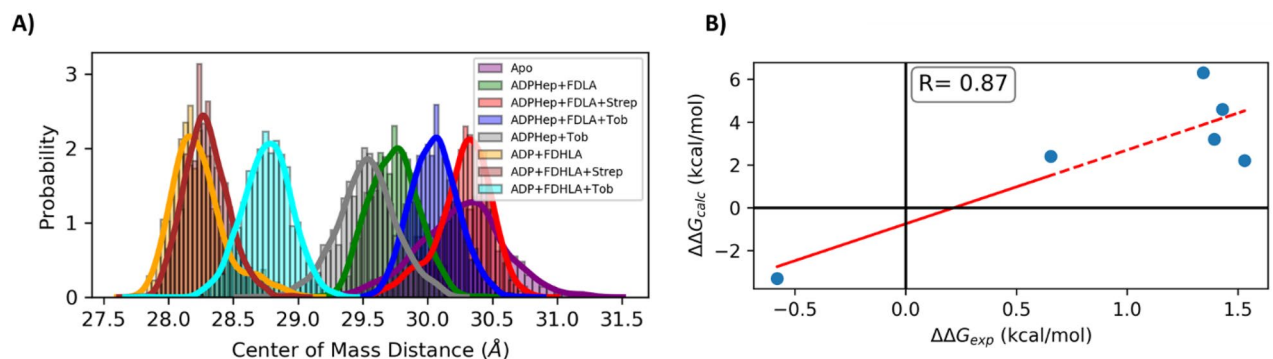


Figure 8. (A) Probability distribution of center of mass distance between N and C termini of HepI in the apo (purple), substrate (green), substrates with Streptomycin (red), substrates with Tobramycin (blue), HepI binary with Tobramycin (grey), products (orange), products with Streptomycin (brown), and products with Tobramycin (cyan). (B) Binding free energy differences of Tobramycin/Streptomycin to HepI WT relative to ARG/LYS mutants.

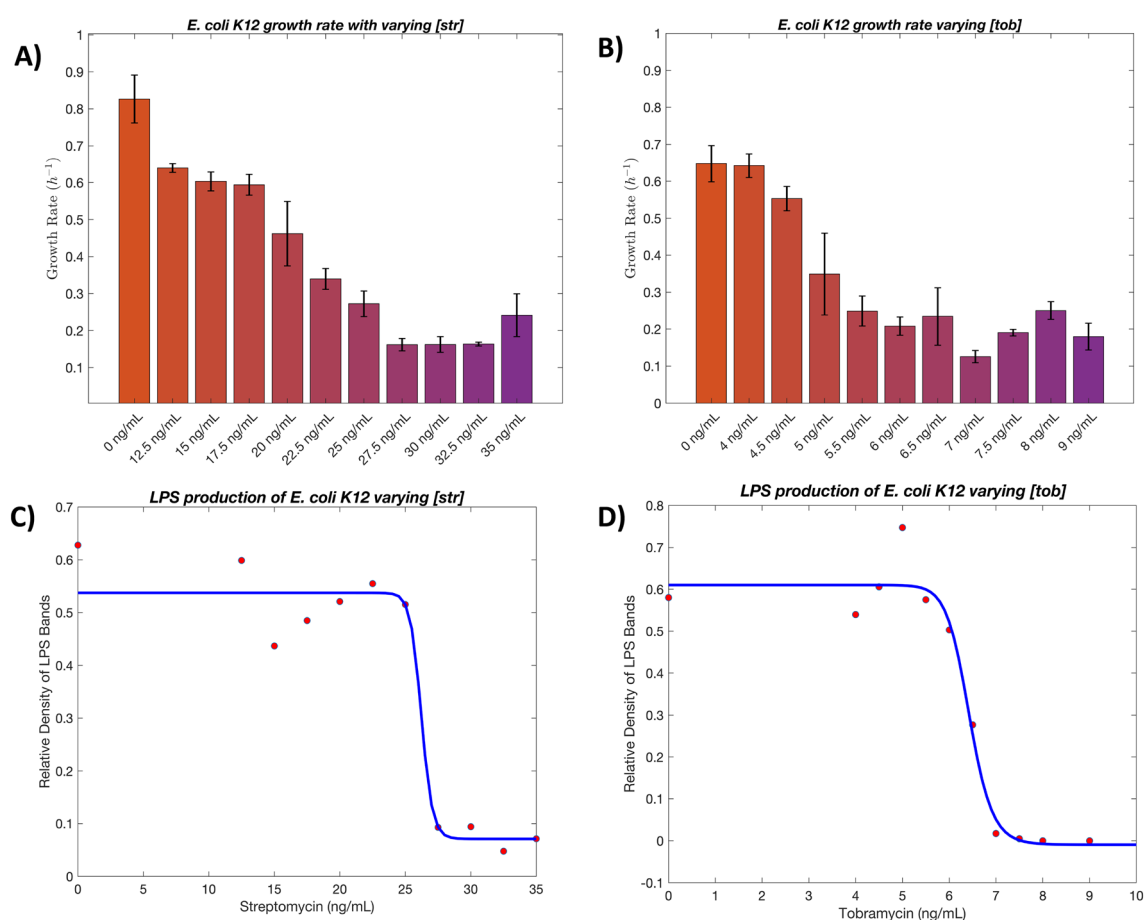


Figure 9. (A) and (B) Calculated growth rate in absorbance increase per hour as determined by the first derivative of a growth curve for streptomycin and tobramycin respectively. Samples from the growth assay are processed and ran on a polyacrylamide gel where the pixel density of LPS bands were determined over the various concentrations and plotted as sigmoid curves for streptomycin (C) and tobramycin (D). IC_{50} values were determined from the inflection point of these fittings at 6.4 ± 0.1 and 26.2 ± 1.0 ng/mL for tobramycin and streptomycin respectively.

the simulations above (Fig. 5B). Since there are no changes to the blue shift due to the addition of inhibitor, and we hypothesize that the loops enriched with positive charges are still able to rearrange to accommodate ODLA.

Over the course of the simulation, streptomycin does not affect the secondary structure of the protein, whereas tobramycin influences this secondary structure and the ability of HepI to close (reduced diameter of the enzyme). Therefore, these inhibitors mostly leave the HepI•ODLA complex formation unaffected, yet they have different

effects on the global conformational change induced by ODLA binding. Examination of the impact of these inhibitors on the circular dichroism studies and thermal stability of HepI•ODLA complex similarly recapitulate these differences in inhibition mechanism. While the overall CD spectra of the enzyme-substrates complexes at 10 °C in the presence and absence of inhibitors were nearly identical, notable differences in the overall thermal stability between these inhibitors were observed. Where a competitive inhibitor would completely disrupt the binding of ODLA to its binding site, tobramycin partially competes for binding to the ODLA site only causing partial destabilization of the HepI•ODLA complex, a > 30 °C difference in melting temperature. This effect is not observed for streptomycin, consistent with its non-competitive mechanism (Fig. 4).

As described previously in detail, the thermal stability of HepI with ODLA is a phenomenon observed frequently with other sugar binding proteins shown through a variety of biophysical methods. Pace et al. in 1979 published the findings of lysozyme thermal stabilization of 5 °C from apo with its native substrate tri-N-acetylglucosamine which, was demonstrated through thermal and guanidine hydrochloride denaturation experiments with and without substrate²⁷. In 1983, Fukada et al. examined the *L*-arabinose binding protein through isothermal and scanning calorimetry experiments to thus discover a similar stabilization phenomenon of a 4 °C increase while in the presence of native substrates *L*-arabinose and *D*-galactose²⁸. In 2001, Wurth et al. utilized our same biophysical methods of CD thermal spectroscopy and intrinsic tryptophan fluorescence as well as x-ray crystallography on thymidine kinase of herpes simplex virus type 1 to discover yet the same phenomenon²⁹. Thymidine kinase of this variety is thermally stabilized by thymidine with or without ATP present and also experiences a blue shifted emission spectra (9 nm in comparison to apo) in the presence of thymidine with ATP. Thymidine kinase with thymidine alone was thermally stabilized by 10 °C and with thymidine and ATP it was thermally stabilized by 20 °C in comparison to apo. We hypothesize that binding interactions between certain native sugar substrates and their proteins generate dramatic conformational rearrangements that induce rigidity within the protein core and delay unfolding events as a result of the sugars' intrinsic quality of solvent rearrangement. In unpublished works, drastic thermal stabilization upon substrate binding has been observed in other GT-B enzymes, with T_m changes by similar magnitude, with further studies needed to discern the conformational changes associated with the biophysical properties of these enzymes.

Additionally, thermal melt experiments in the absence of ODLA showed that the HepI•streptomycin complex destabilized the enzyme evident by an increase of about 15–20% of the unfolding in comparison to the apo with no changes in T_m . This protein destabilization was also observed in HepI•ADPH, HepI•ADP, HepI•tobramycin, HepI•tobramycin•ADP/H, HepI•streptomycin•ADP/H complexes (Supplemental Fig. 7A,C). Based on our experimental and computational findings, thus far, we hypothesize that this phenomenon appears due to a disruption in intrinsic electrostatic interactions within the protein that prevent it from fully unfolding in the apo form which is facilitated by the excess charges introduced by these respective ligands. In the case of a conformational change like that of HepI, the burial of charges has a high desolvation penalty and proteins overcome this barrier by neutralizing through charge pairing or protonation/deprotonation events³⁰. In terms of stability, paired charges increase the stability of a protein due to the strength of electrostatic interactions. We therefore hypothesize that the paired positive charges introduced by streptomycin near the N₃ loop have no net effect on the stabilization that results from the HepI and ODLA complex or the desolvation barrier for closing. However, the excess positive charge introduced by tobramycin into the N₅ loop region effects the HepI•ODLA complex by increasing the desolvation barrier and preventing the full closure while also disrupting the stabilization effect of the neutralized charges through electrostatic repulsion.

The perturbation in LPS production in our in vivo studies are concentration dependent and results in increased sensitivity of the cells. As shown in the bar graph in Fig. 9, tobramycin at around 6.5 ng/mL and streptomycin at 25 ng/mL demonstrate an inflection point in cell viability that has a significant effect on LPS production on the surface. Using the Image J software to analyze the silver-stained polyacrylamide gels, a clear increase in a high molecular mass extracellular polysaccharides was observed (perhaps attributable to capsular polysaccharide, CPS, or colonic acid, but further studies are necessary to fully elucidate the identity of this polysaccharide; Supplemental Table 4) followed by a subsequent decrease is shown, as the LPS production dwindled, which suggests that protein machinery are being hyper utilized for overproduction of a compensatory polysaccharide on the surface to make up for the lack of LPS. The subsequent decrease in high molecular mass surface polysaccharide concentrations could be due to severe lack of LPS which will decrease the membrane integrity making it inherently difficult for other molecules to be installed in the outer membrane.

In prior studies on *E. coli* strains deficient in HepI, notable decreases in cell surface integrity and cell morphology have been observed³¹. These changes on the membrane increase cell susceptibility due to lack of LPS transport onto the surface which subsequently creates pores or openings within the membrane, increasing membrane permeability drastically and in certain strains is fatal to the cell. To compensate, the cell may overexpress other extracellular polymeric substances like CPS to conceal the surface. Pore development in aminoglycoside treated bacteria has been shown previously^{24,32,33} and based on the data demonstrated here with HepI inhibition, we propose that aminoglycoside induced pore development is due to lack of LPS expression on the surface.

Conclusions

This small library of aminoglycosides belong to a potent class of antimicrobial drugs, which can be used alone or as a combinatorial therapy against aerobic Gram-negative and a select few Gram-positive bacterial infections. While the preponderance of prior research has hypothesized that the aminoglycoside antimicrobial activity is conferred by their binding to various locations on the ribosome and the mistranslation of integral membrane proteins, the studies by Rivera et al. revealed that aminoglycosides only slow ribosomal protein activity, and that they are ultimately still productive²⁵. In vivo studies of aminoglycoside action^{22,23,33} demonstrate that “pores” rapidly develop on the bacterial membrane which was previously attributed to alterations in protein translation

and insertion into the membrane. We note that both of these sets of prior observations are consistent with the inhibition of LPS biosynthesis, and since the rate of translation and installation of membrane proteins is far slower than the rate of LPS biosynthesis, the disruption of LPS biosynthesis, through the inhibition of HepI, is a more consistent interpretation of these results. In cells deficient in the genes for HepI⁹, the disruption of LPS biosynthesis causes a reduction in the extracellular polymeric substances embedded on the outer leaflet of the bacteria which could cause the formation of “pores” on the bacterial surface (often described as a deep rough phenotype). With data given above that demonstrates the *in vitro* and *in vivo* inhibition of HepI by aminoglycosides, we hypothesize that the bactericidal mechanism of action of these antimicrobials includes interruption of LPS biosynthesis which may be an important mechanism of aminoglycoside action.

Experimental procedures

Substrate isolation and deacylation. ADPH and Kdo₂-Lipid A isolations have been previously reported³⁴. ADPH and Kdo₂-Lipid A were extracted from *E. coli* WBB06 cells (HepI and HepII knockout *E. coli* strain). Overnight cultures were started by inoculating 10 mL of LB-Tet with WBB06 cells from a glycerol stock stored at -80 °C. LB-Tet media (8 L) was inoculated (1 mL of overnight growth per 2 L of media) and allowed to grow at 37 °C to an OD₆₀₀ of 1 (approximately 12 h), then centrifuged for 10 min at 5,000 rpm to pellet the cells. ADPH was extracted by adding 80 mL of 50% ethanol to the pellet and stirred on ice for 2 h. In 30 mL Nalgene tubes, cells were centrifuged for 20 min at 10,000 rpm and supernatant was saved and the ethanol was removed by vacuum on ice. The crude extract was ultracentrifuged for 1 h at 40,000 rpm and filtered successively using Amicon Ultra-15 30 kDa, 10 kDa and 3 kDa centrifugal filters. Finally, the flow through was placed over a 64 mL DEAE column using a triethylamine bicarbonate (pH=8) gradient from 1–500 mM to purify, crude ADPH and water were also brought to a pH of 8. Approximately 500 µL of each fraction were lyophilized and ESI-mass spectrometry was used to determine fractions that contained pure ADPH by observation of a peak at ($m/z^{-1} = 619$) in a 50:50 acetonitrile:water solution. Fractions confirmed to contain ADPH were pooled and lyophilized successively to remove traces of triethylamine.

Kdo₂-Lipid A was extracted from 8 L of frozen or fresh WBB06 cells grown as described for ADPH extraction. The cells were resuspended in 80 mL of water and the mixture was divided into 30 mL Kimble glass tubes (10 mL per tube) and centrifuged for 10 min at 5,000 rpm. The supernatant was discarded and cells were washed with 160 mL ethanol followed by 160 mL of acetone twice and finally 160 mL of diethyl ether by cellular resuspension in each of the solvents and centrifugation to discard the supernatant before the next wash. Cells were then left to dry in the hood at room temperature 1 h-overnight in a large weigh boat. Kdo₂-Lipid A was then extracted from the dried down cells by pulverizing the cells into a fine powder and adding 20 mL of a solution per tube of 2:5:8 phenol, chloroform, and petroleum ether to 1 g of cells per 30 mL tube. The mixture was vortexed for 3–5 min, left on a nutator for 10 min, then centrifuged for 5,000 rpm for 10 min. Supernatant was gravity filtered through filter paper and the extraction was repeated. The diethyl ether and chloroform was removed in vacuo from the supernatant and a mixture of 75 mL acetone, 15 mL diethyl ether and 5 drops of water was added to the solution and left to sit for 45 min-overnight to precipitate the Kdo₂-Lipid A. The solution was centrifuged at 5,000 rpm for 10 min in 30 mL glass tubes and supernatant was discarded. Pellets were washed a minimum of 3 times with ~ 1 mL 80% phenol and diethyl ether each separately; solutions were centrifuged in between washes and supernatant was removed prior to next wash. The pellets will dramatically diminish over the course of the washes and become more colorless. The dried pellets were then dissolved in 0.5% triethylamine aqueous solution and flash frozen for lyophilization (yield ~ 50 mg).

Synthesis of ODLA has previously been reported³⁵. Briefly, O-deacylation of Kdo₂-Lipid A was done by refluxing a mixture of 5 mL hydrazine to 50 mg of extracted Kdo₂-Lipid A for 1 h at 37 °C in a round-bottom flask with stirring (1 mL of hydrazine for every 10 mg of Kdo₂-Lipid A). The solution was then placed on ice and 10 mL cold acetone was added for every 1 mL hydrazine to precipitate ODLA followed by centrifugation for 30 min at 11,000 rpm. The pellet was washed 3 times each with cold acetone and diethyl ether; solvent was carefully decanted. After allowing the diethyl ether to evaporate ~ 5 min on its side under the fume hood, the pellets were dissolved in water and pooled together, flash frozen and lyophilized. Deacylation was confirmed by ESI-mass spectroscopy in 50:50 acetonitrile:water by observation of the half mass ($m/z^{-2} = 695$).

HepI expression and purification. HepI cloned from the *E. coli* K12 strain MB1760 (*Escherichia coli* ATCC 19,215) was expressed in *E. coli* One Shot BL-21-AI as described previously with some changes. Two liters of LB-Amp media was inoculated with 10 mL of an overnight culture and allowed to grow at 37 °C, 200 rpm until an OD₆₀₀ of 0.4–0.8 was reached (approximately 3–5 h). The cells were induced to a final concentration of 1 mM IPTG and 0.002% *L*-arabinose at 30 °C and expressed for 24 h. Cells were harvested by centrifugation for 10 min at 5,000 rpm. Supernatant was discarded and cell pellets were re-dissolved in 20 mL of binding buffer (20 mM HEPES, 1 mM imidazole and 500 mM NaCl, pH 7.4) for every liter of grown culture, to which ~ 1 mg of lysozyme was also added to aid in the lysing of cells. Cells were incubated on ice while mixing for 30 min, followed by homogenization at 18,000 psi for 5–10 cycles. The lysate was clarified by centrifugation at 13,000 rpm for 1 h and the supernatant was loaded on to a Toyopearl AF-chelate-640 column attached to an ÄKTA purifier stored at 4 °C. The purification method charges the column with 500 µM cobalt sulfate, equilibrates with binding buffer, then protein is loaded and washed again with binding buffer. To remove any unbound protein the column was washed with wash buffer (20 mM HEPES, 40 mM imidazole and 500 mM NaCl, pH 7.4). Finally, HepI is eluted with strip buffer (50 mM ethylenediaminetetraacetic acid (EDTA) and 500 mM NaCl, pH 6.8).

To determine which samples contained HepI, SDS-PAGE gels stained with Coomassie blue stain were used to determine which fractions contain the 37 kDa protein (HepI). HepI consistently is co-eluted in the strip buffer with cobalt; fractions were pooled together and concentrated using 10,000 MWCO Vivaspın Ultra centrifugal

concentrator. Concentrated (~5–10 mL) HepI was then placed over Bio-Scale Mini Bio-Gel P-6 desalting cartridge to buffer exchange into HepI storage buffer (100 mM HEPES, 1 M KCl, pH 7.5), column was also attached to an Äkta purifier at 4 °C. Again, fractions that contained purified protein were combined and concentrated using 10,000 MWCO Vivaspin Ultra centrifugal concentrator.

Protein was then stored in an amber, glass vial as a 50% ammonium sulfate precipitate at 4 °C. Protein remains stable for a few months after purification. To use for desired assay, precipitate was centrifuged at 4 °C for 6 min at 13,000 rpm, supernatant was removed and pellet was dissolved in desired buffer depending on experiment(s) to be carried out. Concentration was determined via nanodrop using the absorbance at 280 nm, and Beer's law was employed to determine concentration given the extinction coefficient of HepI 55,928 M⁻¹ cm⁻¹.

Enzymatic assays. As previously reported^{11,14,15}, an ADP/NADH coupled assay was used to monitor HepI activity by monitoring the absorbance change at 340 nm at 37 °C on a Cary Bio 100 UV-Vis Spectrometer. Under normal conditions, the assay buffer was composed of 50 mM HEPES, 50 mM KCl, 10 mM MgCl₂, pH 7.5. The coupled enzyme reaction additionally contained 100 μM phosphoenolpyruvate, 100 μM NADH, 100 μM dithiothreitol (DTT) and 0.05 U/μL of both pyruvate kinase and lactate dehydrogenase. 100 μM ADPH was used when ODLA concentration was varied and 100 μM ODLA was used when ADPH was varied. Once a stable baseline was established (~5 min), the reaction was initiated by addition of HepI to a final concentration of 50 nM or 100 nM (for high and lower substrate concentrations respectively) and all reported reaction rates are after background subtraction. When running 12 samples at once, plastic cuvette stirs and a repeat pipettor was used to inject 200 μL enzyme. Inhibition of HepI was monitored using the same ADP/NADH coupled assay, all conditions of the assay were the same as previously described unless otherwise stated. *K_i* values for each of the compounds were determined by varying compound final concentration from 100 μM to 10 nM, and a final concentration of 10 μM ODLA. Competition assays against ADPH were done with excess ODLA (100 μM) and varying ADPH from 2–0.25 μM. Competition assays against ODLA were done with excess ADPH (100 μM) and varying ODLA from 2–0.25 μM. Reactions were started with addition of enzyme and inhibitor was varied from 30–0.01 μM. Kinetics were fit to Lineweaver-Burke (Eq. 1), competitive (Eq. 2), non-competitive (Eq. 3), mixed (Eq. 4), Dixon (Eq. 5), or Cornish-Bowden (Eq. 6) models. All fitting and plotting was done through MATLAB R2018A.

$$\frac{1}{V} \left(\frac{1}{[S]} \right) = \frac{K_M}{V_{\max}[S]} + \frac{1}{V_{\max}} \quad (1)$$

$$V([S]) = \frac{V_{\max}[S]}{K_M \left(1 + \frac{[I]}{K_i} \right) + [S]} \quad (2)$$

$$V([S]) = \frac{V_{\max}[S] / \left(1 + \left(\frac{[I]}{K_i} \right) \right)}{K_M + [S]} \quad (3)$$

$$V([S]) = \frac{V_{\max}[S]}{K_M \left(1 + \frac{[I]}{K_i} \right) + [S] \left(1 + \frac{[I]}{\alpha K_i} \right)} \quad (4)$$

$$\frac{1}{V}([I]) = \frac{K_M \left(1 + \frac{[I]}{K_i} \right) + [S] \left(1 + \frac{[I]}{\alpha K_i} \right)}{V_{\max}[S]} \quad (5)$$

$$\frac{[S]}{V}([I]) = \frac{K_M \left(1 + \frac{[I]}{K_i} \right) + [S] \left(1 + \frac{[I]}{\alpha K_i} \right)}{V_{\max}} \quad (6)$$

Circular dichroism experiments. Circular dichroism melt experiments were performed in a Jasco J-810 spectropolarimeter in Starna 21-Q-2 cells (minimum volume 400 μL) sealed with Teflon tape to prevent evaporation. Parameters include 3 accumulations of data collected between 195–275 nm as a function of temperature (10–95 °C with 5° increments) at a ramp rate of 2°/min and a scanning rate of 50 nm/min. Samples were prepared by diluting a mixture of 5 μM HepI and some combination of 250 μM substrate/product and/or 100 μM inhibitor in a buffer of 10 mM Tris-HCl and 100 mM KCl (pH = 7.5). CD data was analyzed via in house script written in MATLAB R2018A that average a set of triplicate data, normalizes to a percent unfolded (assuming the protein is fully folded at 5 °C) at 222 nm as a function of temperature and fits to a sigmoid curve to determine the melt temperature (*T_M*).

Intrinsic tryptophan fluorescence spectra measurements. Fluorescence spectra were measured in triplicate at room temperature using 200 μL samples containing 1 μM HepI, in a 10 mM HEPES, 50 mM KCl, and 10 mM MgCl₂, pH = 7.5 buffer. Samples were contained in Starna 45-Q-3 cells (minimum volume 200 μL). Substrate and inhibitor concentrations were 100 μM. All measurements were taken using a Fluoromax-4 fluorometer

with an excitation slit bandpass of 2 nm and an emission slit bandpass of 3 nm ($\lambda_{\text{ex}} = 290$ nm, $\lambda_{\text{em}} = 310\text{--}450$ nm). The data was subtracted from blanks, normalized and fit to a lognormal distribution (Eq. 7)³⁶ to determine the emission maximum (λ_{max}) with in house scripts written in MATLAB R2018A.

$$I(\lambda) = I_{\text{max}} \cdot e^{\left\{ -\frac{\ln^2 \rho}{\ln^2 \rho} \cdot \ln^2 \left(\frac{a-\lambda}{a-\lambda_{\text{max}}} \right) \right\}} \quad (7)$$

Docking. HepI model system for docking and molecular dynamic simulations were prepared as previously described. Briefly, the HepI•ADPHep binary complex was modeled with the previously solved structure (PDB: 2H1H)¹¹. The ADP-2-deoxy-2-fluoro heptose present in this structure was modified to mimic the native donor via replacement of the 2-fluoro group with a hydroxyl group and inversion of the stereo configuration. The ternary complex was modeled with the previously solved pseudo-ternary complex (PDB: 6DFE)²⁶. This structure contains a native acceptor analogue with acyl chains replaced by singular acyl groups at the N positions of the terminal glucosamines. Furthermore, the acceptor is a phosphonate derivate and was replaced with the modified native donor from the HepI•ADPH binary complex described above.

Structures were prepared in Maestro with the protein preparation wizard and provided default settings³⁷. Missing loops and sidechains were modeled with Prime and protonation states were determined with PROPKA^{38–41}. Docking was carried out in Glide with standard precision and the OPLS3e forcefield^{42,43}. The protein was held rigid and the ligand was flexible to sample the possible conformational space of optimal binding poses. The 10 lowest energy poses, as determined by the Glide docking score, were energy minimized and subject to MMGBSA end point free energy approximation. The lowest binding energy pose was selected for molecular dynamic simulations^{44,45}. Streptomycin and Tobramycin were docked to the HepI•ADPHep•FDLA complex. Tobramycin was also docked to the HepI•ADPHep complex to explore the competitive nature of Tobramycin towards FDLA as determined by kinetics.

Molecular dynamic simulations. Molecular dynamic simulations were implemented in the GROMACS 2021.1⁴⁶ package with the AMBER99SB forcefield⁴⁷. Ligands were parametrized with antechamber from AmberTools20⁴⁸. Atom types were assigned from the second generation general AMBER forcefield (GAFF2) and charges were applied with the AM1-BCC method⁴⁹. Resulting files were converted to Gromacs compatible file formats with the ACPYPE script⁵⁰. The protein ligand complexes were placed into a dodecahedron with periodic boundary condition solvated with the TIP3P water model⁵¹. The system was electroneutralized with the addition of counterions and subsequent addition of ions to a concentration of 0.150 M to mimic physiological conditions. The steepest decent algorithm was used for energy minimization. The system was further equilibrated with subsequent 1 ns simulations under isochoric/isothermal (NVT) and isobaric/isothermal (NPT) conditions. During equilibration harmonic restraints (1000 kJ/mol/nm²) were applied to all heavy atoms and gradually removed in a stepwise fashion, initially from sidechains then the backbone, over the course of 10 ns. Production simulations were carried out for 100 ns in triplicate under isobaric/isothermal (NPT) conditions with a 2 fs timestep at 300 K and 1 atm. Long range electrostatic interactions were calculated with the particle-mesh-Ewald with a fourth order cubic interpolation and a 1.6 Å grid spacing. Short range nonbonded interactions were calculated with a 10 Å cutoff. Temperature was maintained with the V-rescale thermostat, while pressure was maintained with the Berendsen and Parrinello-Rahman barostat during equilibration or production simulations, respectively^{52–55}. Bonds were constrained with the LINCS method⁵⁶. Root mean square deviation (RMSD) of the protein backbone and root mean square fluctuations (CaRMSF) of the Ca were calculated in GROMACS for individual trajectories. Averages and standard deviations of the RMSD and CaRMSF were calculated and plotted via Python⁵⁷.

Binding free energies. Binding energies of inhibitors to the protein/substrate ternary complex were determined by the molecular mechanics poisson boltzman solvent accessible (MMPBSA) method in Amber using the MMPBSA.py script and gmx_MMPBSA extension with an internal dielectric constant of 4^{58,59}. The binding energies and its standard deviation were evaluated from 300 representative frames taken at 100 ps time interval for each of the three 100 ns simulated trajectories. Experimental binding energies of the inhibitors to the protein/substrate complex were estimated with the Gibbs Free Energy equation and the equilibrium constant approximated as K_i . Both values were plotted as a function of another and fit to straight line to determine a correlation value.

Cell-based assays and LPS visualization gels. The assays were prepared by plating *E. coli* K12 onto an LB-agar plate and grown overnight (12–18 h)⁶⁰. A colony forming unit was chosen to inoculate 10 mL of fresh LB media in a tightly capped 15 mL falcon tube and placed in an incubator (no agitation) at 37 °C for exactly 24 h to increase the number of viable cells for inoculation of the plate and thusly reproducibility in highly variable growth patterns. A 96-well plate was then filled with a variety of inhibitor concentrations taken from stock solutions made up in ultra-pure water allowing for one row to remain free of the inhibitor. Each inhibitor concentration was given 3-wells to ensure a triplicate of data is collected at once. With the same fresh media used to make the overnight culture, the overnight growths were added to the plate in a 1:1000 dilution (total volume 200 μ L) and the plate sealed with clear adhesive plastic sealant. One row has been designated for uncultured media to be used for pre-blanking measurements and to ensure that the media isn't growing spontaneously.

An experimental protocol was created using the Softmax Pro® software for a Molecular Devices Spectramax M5 plate reader. The parameters have been selected such that it collects pre-blanked absorbance readings at 600 nm wavelengths every 30 min at 37 °C with shaking every 10 min at 400 s intervals for 18 h total. Absorbance

values were corrected for path length using the lateral reading path correction (8) and are plotted overtime to establish a growth curve.

$$l = 4 \times V/\pi \times d^2 \quad (8)$$

l = path length from Beer's law ($A = \epsilon lc$), V = volume (cm^3), d = diameter of well (cm).

As previously established, lipid extraction occurs through lysis of surface polysaccharides with a lysis buffer containing 1% SDS, 20% glycerol, 100 mM Tris-HCl and 0.04% bromophenol blue at a pH 6.8⁶¹. The cellular concentrations from each well were determined using the last collected OD₆₀₀ corrected using Eq. (8), centrifuged and resuspended in the correct volume of lysis buffer to obtain 4×10^8 cells/100 μL solution. Addition of Proteinase K at 1 mg/mL concentration was incubated for 1 h at 37 °C. These samples were then loaded onto a 15% separating, 6% stacking SDS-polyacrylamide gel (recipes received from <https://www.bio-rad.com/>) in a 19:1 acrylamide to bis-acrylamide ratio and run with a voltage gradient from 50–150 V. The gels were then stained using the protocol described previously with no modifications⁶² and imaged using a scanner.

Data from the growth assay were analyzed using MATLAB R2018A. The derivative of the curve was calculated and the maximum rate as determined by the derivative was reported as the growth rate for that condition.

Relative LPS band density was determined using analysis methods provided by ImageJ software. The band pixel density were analyzed relative to a purified sample of heptosylated O-deacylated Lipid A at 100 nM. The plot was generated of relative band density vs. concentration of inhibitor⁶³.

Data availability

The data underlying this article are available in the article and in its online supplementary material. Software used in this study are available from their respective sources. Scripts and simulation trajectories are available from the corresponding authors upon request.

Received: 7 November 2021; Accepted: 4 April 2022

Published online: 04 May 2022

References

- Munita, J. M. & Arias, C. A. Mechanisms of antibiotic resistance. *Microbiol. Spectr.* **4**, 2015. <https://doi.org/10.1128/microbiolspec.VMBF-0016-2015> (2016).
- Hankins, J. V., Madsen, J. A., Needham, B. D., Brodbelt, J. S. & Trent, M. S. The outer membrane of Gram-negative bacteria: Lipid A isolation and characterization. *Methods Mol. Biol.* **966**, 239–258. https://doi.org/10.1007/978-1-62703-245-2_15 (2013).
- Frieri, M., Kumar, K. & Boutin, A. Antibiotic resistance. *J. Infect. Public Health* **10**, 369–378. <https://doi.org/10.1016/j.jiph.2016.08.007> (2017).
- Davies, J. & Davies, D. Origins and evolution of antibiotic resistance. *Microbiol. Mol. Biol. Rev.* **74**, 417. <https://doi.org/10.1128/MMBR.00016-10> (2010).
- Alexander, C. & Rietschel, E. T. Invited review: Bacterial lipopolysaccharides and innate immunity. *J. Endotoxin Res.* **7**, 167–202. <https://doi.org/10.1177/09680519010070030101> (2001).
- Raetz, C. R. H. & Whitfield, C. Lipopolysaccharide endotoxins. *Annu. Rev. Biochem.* **71**, 635–700. <https://doi.org/10.1146/annurev.biochem.71.110601.135414> (2002).
- Moreau, F. *et al.* Discovery of new Gram-negative antivirulence drugs: Structure and properties of novel *E. coli* WaaC inhibitors. *Bioorg. Med. Chem. Lett.* **18**, 4022–4026. <https://doi.org/10.1016/j.bmcl.2008.05.117> (2008).
- Gunn, J. S. Bacterial modification of LPS and resistance to antimicrobial peptides. *J. Endotoxin Res.* **7**, 57–62. <https://doi.org/10.1177/09680519010070011001> (2001).
- Cote, J. M. & Taylor, E. A. The glycosyltransferases of LPS Core: A review of four heptosyltransferase enzymes in context. *Int. J. Mol. Sci.* **18**, 2256. <https://doi.org/10.3390/ijms18112256> (2017).
- Mamat, U., Skurnik, M. & Bengoechea, J. A. in *Bacterial Lipopolysaccharides: Structure, Chemical Synthesis, Biogenesis and Interaction with Host Cells* (eds Yuriy A. Knirel & Miguel A. Valvano) 237–273 (Springer Vienna, 2011).
- Grizot, S. *et al.* Structure of the *Escherichia coli* Heptosyltransferase WaaC: Binary Complexes with ADP AND ADP-2-deoxy-2-fluoro Heptose. *J. Mol. Biol.* **363**, 383–394. <https://doi.org/10.1016/j.jmb.2006.07.057> (2006).
- Anderson, A. C. The process of structure-based drug design. *Chem. Biol.* **10**, 787–797. <https://doi.org/10.1016/j.chembiol.2003.09.002> (2003).
- Tikad, A. *et al.* Mechanistic insight into heptosyltransferase inhibition by using Kdo multivalent glycoclusters. *Chem. Eur. J.* **22**, 13147–13155. <https://doi.org/10.1002/chem.201602190> (2016).
- Nkosana, N. K., Czyzyk, D. J., Siegel, Z. S., Cote, J. M. & Taylor, E. A. Synthesis, kinetics and inhibition of *Escherichia coli* Heptosyltransferase I by monosaccharide analogues of Lipid A. *Bioorg. Med. Chem. Lett.* **28**, 594–600. <https://doi.org/10.1016/j.bmcl.2018.01.040> (2018).
- Czyzyk, D. J., Sawant, S. S., Ramirez-Mondragon, C. A., Hingorani, M. M. & Taylor, E. A. *Escherichia coli* Heptosyltransferase I: Investigation of protein dynamics of a GT-B structural enzyme. *Biochemistry* **52**, 5158–5160. <https://doi.org/10.1021/bi400807r> (2013).
- Cote, J. M. *et al.* The stories tryptophans tell: Exploring protein dynamics of heptosyltransferase I from *Escherichia coli*. *Biochemistry* **56**, 886–895. <https://doi.org/10.1021/acs.biochem.6b00850> (2017).
- Cote, J. M. *et al.* Opposites attract: *Escherichia coli* heptosyltransferase I conformational changes induced by interactions between the substrate and positively charged residues. *Biochemistry* **59**, 3135–3147. <https://doi.org/10.1021/acs.biochem.9b01005> (2020).
- Ramirez-Mondragon, C. A. *et al.* Conserved conformational hierarchy across functionally divergent glycosyltransferases of the GT-B structural superfamily as determined from microsecond molecular dynamics. *Int. J. Mol. Sci.* **22**, 4619. <https://doi.org/10.3390/ijms22094619> (2021).
- Hassan, B. A., Milicaj, J., Sham, Y. Y. & Taylor, E. A. Ligand induced conformational and dynamical changes in a GT-B glycosyltransferase: Molecular dynamic simulations of heptosyltransferase I Apo, binary and ternary complexes. *bioRxiv* <https://doi.org/10.1101/2021.06.16.448588> (2021).
- Davis, B. D., Chen, L. L. & Tai, P. C. Misread protein creates membrane channels: an essential step in the bactericidal action of aminoglycosides. *Proc. Natl. Acad. Sci. U. S. A.* **83**, 6164–6168. <https://doi.org/10.1073/pnas.83.16.6164> (1986).
- Nichols, W. W. & Young, S. N. Respiration-dependent uptake of dihydrostreptomycin by *Escherichia coli*. Its irreversible nature and lack of evidence for a uniport process. *Biochem. J.* **228**, 505–512. <https://doi.org/10.1042/bj2280505> (1985).

22. Krause, K. M., Serio, A. W., Kane, T. R. & Connolly, L. E. Aminoglycosides: An overview. *Cold Spring Harb. Perspect. Med.* **6**, a027029. <https://doi.org/10.1101/cshperspect.a027029> (2016).
23. Davis, B. D. Mechanism of bactericidal action of aminoglycosides. *Microbiol Rev* **51**, 341–350. <https://doi.org/10.1128/mr.51.3.341-350.1987> (1987).
24. Vaara, M. Agents that increase the permeability of the outer membrane. *Microbiol. Rev.* **56**, 395–411. <https://doi.org/10.1128/mr.56.3.395-411.1992> (1992).
25. Aguirre Rivera, J. *et al.* Real-time measurements of aminoglycoside effects on protein synthesis in live cells. *Proc. Natl. Acad. Sci.* **118**, e2013315118. <https://doi.org/10.1073/pnas.2013315118> (2021).
26. Blaukopf, M., Worrall, L., Kosma, P., Strynadka, N. C. J. & Withers, S. G. Insights into heptosyltransferase I catalysis and inhibition through the structure of its ternary complex. *Structure* **26**, 1399–1407. <https://doi.org/10.1016/j.str.2018.07.001> (2018).
27. Pace, C. N. & McGrath, T. Substrate stabilization of lysozyme to thermal and guanidine hydrochloride denaturation. *J. Biol. Chem.* **255**, 3862–3865 (1980).
28. Fukada, H., Sturtevant, J. M. & Quioco, F. A. Thermodynamics of the binding of *L*-arabinose and of *D*-galactose to the *L*-arabinose-binding protein of *Escherichia coli*. *J. Biol. Chem.* **258**, 13193–13198 (1983).
29. Würth, C. *et al.* The effect of substrate binding on the conformation and structural stability of Herpes simplex virus type 1 thymidine kinase. *Protein Sci* **10**, 63–73. <https://doi.org/10.1110/ps.27401> (2001).
30. Zhou, H.-X. & Pang, X. Electrostatic interactions in protein structure, folding, binding, and condensation. *Chem. Rev.* **118**, 1691–1741. <https://doi.org/10.1021/acs.chemrev.7b00305> (2018).
31. Nikaido, H. Molecular basis of bacterial outer membrane permeability revisited. *Microbiol. Mol. Biol. Rev.* **67**, 593–656. <https://doi.org/10.1128/mmr.67.4.593-656.2003> (2003).
32. Peterson, A. A., Hancock, R. E. W. & McGroarty, E. J. Binding of polycationic antibiotics and polyamines to lipopolysaccharides of *Pseudomonas aeruginosa*. *J. Bacteriol* **164**, 1256–1261 (1985).
33. Moore, R. A., Bates, N. C. & Hancock, R. E. Interaction of polycationic antibiotics with *Pseudomonas aeruginosa* lipopolysaccharide and lipid A studied by using dansyl-polymyxin. *Antimicrob. Agents Chemother.* **29**, 496–500. <https://doi.org/10.1128/aac.29.3.496> (1986).
34. Milicaj, J., Castro, C. D., Jaunbocus, N. & Taylor, E. A. Extraction of ADP-heptose and Kdo2-lipid A from *E. coli* deficient in the heptosyltransferase I gene. *Appl. Sci.* **11**, 8314 (2021).
35. Czyzyk, D. J., Liu, C. & Taylor, E. A. Lipopolysaccharide biosynthesis without the lipids: recognition promiscuity of *Escherichia coli* heptosyltransferase I. *Biochemistry* **50**, 10570–10572. <https://doi.org/10.1021/bi201581b> (2011).
36. Hixon, J. & Reshetnyak, Y. K. Algorithm for the analysis of tryptophan fluorescence spectra and their correlation with protein structural parameters. *Algorithms* **2**, 1155–1176. <https://doi.org/10.3390/a2031155> (2009).
37. Madhavi Sastry, G., Adzhigirey, M., Day, T., Annabhimoju, R. & Sherman, W. Protein and ligand preparation: parameters, protocols, and influence on virtual screening enrichments. *J. Comput. Aided Mol. Des.* **27**, 221–234. <https://doi.org/10.1007/s10822-013-9644-8> (2013).
38. Olsson, M. H. M., Sondergaard, C. R., Rostkowski, M. & Jensen, J. H. PROPKA3: Consistent treatment of internal and surface residues in empirical pKa predictions. *J. Chem. Theory Comput.* **7**, 525–537. <https://doi.org/10.1021/ct100578z> (2011).
39. Sondergaard, C. R., Olsson, M. H. M., Rostkowski, M. & Jensen, J. H. Improved treatment of ligands and coupling effects in empirical calculation and rationalization of pKa values. *J. Chem. Theory Comput.* **7**, 2284–2295. <https://doi.org/10.1021/ct200133y> (2011).
40. Jacobson, M. P. *et al.* A hierarchical approach to all-atom protein loop prediction. *Proteins Struct. Funct. Bioinform.* **55**, 351–367. <https://doi.org/10.1002/prot.10613> (2004).
41. Jacobson, M. P., Friesner, R. A., Xiang, Z. & Honig, B. On the role of the crystal environment in determining protein side-chain conformations. *J. Mol. Biol.* **320**, 597–608. [https://doi.org/10.1016/S0022-2836\(02\)00470-9](https://doi.org/10.1016/S0022-2836(02)00470-9) (2002).
42. Friesner, R. A. *et al.* Glide: A new approach for rapid, accurate docking and scoring. 1. Method and assessment of docking accuracy. *J. Med. Chem.* **47**, 1739–1749. <https://doi.org/10.1021/jm0306430> (2004).
43. Roos, K. *et al.* OPLS3e: Extending force field coverage for drug-like small molecules. *J. Chem. Theory Comput.* **15**, 1863–1874. <https://doi.org/10.1021/acs.jctc.8b01026> (2019).
44. Genheden, S. & Ryde, U. The MM/PBSA and MM/GBSA methods to estimate ligand-binding affinities. *Expert Opin. Drug Discov.* **10**, 449–461. <https://doi.org/10.1517/17460441.2015.1032936> (2015).
45. Wang, E. *et al.* End-point binding free energy calculation with MM/PBSA and MM/GBSA: Strategies and applications in drug design. *Chem. Rev.* **119**, 9478–9508. <https://doi.org/10.1021/acs.chemrev.9b00055> (2019).
46. Van Der Spoel, D. *et al.* GROMACS: Fast, flexible, and free. *J. Comput. Chem.* **26**, 1701–1718. <https://doi.org/10.1002/jcc.20291> (2005).
47. Hornak, V. *et al.* Comparison of multiple Amber force fields and development of improved protein backbone parameters. *Proteins* **65**, 712–725. <https://doi.org/10.1002/prot.21123> (2006).
48. Pearlman, D. A. *et al.* AMBER, a package of computer programs for applying molecular mechanics, normal mode analysis, molecular dynamics and free energy calculations to simulate the structural and energetic properties of molecules. *Comput. Phys. Commun.* **91**, 1–41. [https://doi.org/10.1016/0010-4655\(95\)00041-D](https://doi.org/10.1016/0010-4655(95)00041-D) (1995).
49. Jakalian, A., Jack, D. B. & Bayly, C. I. Fast, efficient generation of high-quality atomic charges. AM1-BCC model: II. Parameterization and validation. *J. Comput. Chem.* **23**, 1623–1641. <https://doi.org/10.1002/jcc.10128> (2002).
50. Sousa da Silva, A. W. & Vranken, W. F. ACPYPE—AnteChamber PYthon Parser interface. *BMC Res. Notes* **5**, 367–367. <https://doi.org/10.1186/1756-0500-5-367> (2012).
51. Jorgensen, W. L., Chandrasekhar, J., Madura, J. D., Impey, R. W. & Klein, M. L. Comparison of simple potential functions for simulating liquid water. *J. Chem. Phys.* **79**, 926–935. <https://doi.org/10.1063/1.445869> (1983).
52. Berendsen, H. J. C., Postma, J. P. M., van Gunsteren, W. F., DiNola, A. & Haak, J. R. Molecular dynamics with coupling to an external bath. *J. Chem. Phys.* **81**, 3684–3690. <https://doi.org/10.1063/1.448118> (1984).
53. Bussi, G., Donadio, D. & Parrinello, M. Canonical sampling through velocity rescaling. *J. Chem. Phys.* **126**, 014101. <https://doi.org/10.1063/1.2408420> (2007).
54. Parrinello, M. & Rahman, A. Polymorphic transitions in single crystals: A new molecular dynamics method. *J. Appl. Phys.* **52**, 7182–7190. <https://doi.org/10.1063/1.328693> (1981).
55. Parrinello, M. & Rahman, A. Strain fluctuations and elastic constants. *J. Chem. Phys.* **76**, 2662–2666. <https://doi.org/10.1063/1.443248> (1982).
56. Hess, B., Bekker, H., Berendsen, H. J. C. & Fraaije, J. G. E. M. LINCS: A linear constraint solver for molecular simulations. *J. Comput. Chem.* **18**, 1463–1472. [https://doi.org/10.1002/\(SICI\)1096-987X\(199709\)18:12%3C1463::AID-JCC4%3e3.0.CO;2-H](https://doi.org/10.1002/(SICI)1096-987X(199709)18:12%3C1463::AID-JCC4%3e3.0.CO;2-H) (1997).
57. Pilgrim, M. *Dive Into Python 3* (Apress, 2010).
58. Miller 3rd, B. R. *et al.* MMPBSA.py: An efficient program for end-state free energy calculations. *J. Chem. Theory Comput.* **8**, 3314–3321. <https://doi.org/10.1021/ct300418h> (2012).
59. Tresanco, M. S. V., Valdes-Tresanco, M. E., Valiente, P. A. & Frías, E. M. gmx_MMPBSA. <https://doi.org/10.5281/ZENODO.4814044> (2021).
60. Hall, B. G., Acar, H., Nandipati, A. & Barlow, M. Growth rates made easy. *Mol. Biol. Evol.* **31**, 232–238. <https://doi.org/10.1093/molbev/mst187> (2014).

61. Hitchcock, P. J. & Brown, T. M. Morphological heterogeneity among Salmonella lipopolysaccharide chemotypes in silver-stained polyacrylamide gels. *J. Bacteriol.* **154**, 269–277. <https://doi.org/10.1128/jb.154.1.269-277.1983> (1983).
62. Fomsgaard, A., Freudenberg, M. A. & Galanos, C. Modification of the silver staining technique to detect lipopolysaccharide in polyacrylamide gels. *J. Clin. Microbiol.* **28**, 2627–2631. <https://doi.org/10.1128/jcm.28.12.2627-2631.1990> (1990).
63. Andrews, J. M. Determination of minimum inhibitory concentrations. *J. Antimicrob. Chemother.* **48**(Suppl 1), 5–16. https://doi.org/10.1093/jac/48.suppl_1.5 (2001).

Acknowledgements

We would like to acknowledge the University of Minnesota Supercomputing Institute provided the Schrodinger software package for performing the docking studies.

Author contributions

Conceptualization, J.M.C., J.M., B.A.H., C.A.R.M., R.M., Y.Y.S., and E.A.T.; methodology, J.M., B.A.H., J.M.C., A.R., K.R.P., C.D.C., Y.Y.S., and E.A.T.; validation, J.M., B.A.H., Y.Y.S., and E.A.T.; writing—original draft preparation, J.M., B.A.H., and N.J.; writing—review and editing, J.M., B.A.H., Y.Y.S., and E.A.T.; visualization, J.M., and B.A.H.; supervision, project administration, funding acquisition, Y.Y.S., and E.A.T. All authors have read and agreed to the published version of the manuscript.

Funding

This work was funded in part by the National Institutes of Health [Grant # 1R15AI119907-01 to EAT], funding period 05/2016-04/2019.

Competing interests

The authors declare no competing interests.

Additional information

Supplementary Information The online version contains supplementary material available at <https://doi.org/10.1038/s41598-022-10776-x>.

Correspondence and requests for materials should be addressed to Y.Y.S. or E.A.T.

Reprints and permissions information is available at www.nature.com/reprints.

Publisher's note Springer Nature remains neutral with regard to jurisdictional claims in published maps and institutional affiliations.



Open Access This article is licensed under a Creative Commons Attribution 4.0 International License, which permits use, sharing, adaptation, distribution and reproduction in any medium or format, as long as you give appropriate credit to the original author(s) and the source, provide a link to the Creative Commons licence, and indicate if changes were made. The images or other third party material in this article are included in the article's Creative Commons licence, unless indicated otherwise in a credit line to the material. If material is not included in the article's Creative Commons licence and your intended use is not permitted by statutory regulation or exceeds the permitted use, you will need to obtain permission directly from the copyright holder. To view a copy of this licence, visit <http://creativecommons.org/licenses/by/4.0/>.

© The Author(s) 2022